ACS APPLIED NANO MATERIALS

Article

Poly(octadecyl acrylate)-Grafted-Multiwalled Carbon Nanotube Composites for Wearable Temperature Sensors

Alexander Jun Wang, Surendra Maharjan, Kang-Shyang Liao, Brian P. McElhenny, Kourtney D. Wright, Eoghan Dillon, Ram Neupane, Zhuan Zhu, Shuo Chen, Andrew R Barron, Oomman K. Varghese, Jiming Bao, and Seamus A. Curran

ACS Appl. Nano Mater., **Just Accepted Manuscript** • DOI: 10.1021/acsanm.9b02396 • Publication Date (Web): 28 Jan 2020

Just Accepted

is published by the American Chemical Society. 1155 Sixteenth Street N.W., Washington, DC 20036

Poly(octadecyl acrylate)-Grafted Multiwalled Carbon Nanotube Composites for Wearable Temperature Sensors

Alexander J. Wang, [†§] Surendra Maharjan,[†§] Kang-Shyang Liao,[†§] Brian P. McElhenny,[§‡] Kourtney D. Wright,[€] Eoghan P. Dillon,[||] Ram Neupane,[#] Zhuan Zhu,[¥] Shuo Chen,[§‡] Andrew R. Barron,[€] Oomman K. Varghese,[#] Jiming Bao,[¥] and Seamus A. Curran[†§]*

[†]Advanced Manufacturing Institute, University of Houston, 5000 Gulf Freeway, Houston, Texas 77023, USA

[§]Department of Physics, University of Houston, Houston, Texas 77204, USA

[‡]Texas Center for Superconductivity, University of Houston, Houston, Texas 77204, USA

[€]Department of Chemistry, Rice University, Houston, Texas 77005, USA

[||]Anasys Instruments, Santa Barbara, California 93101, USA

[#]Nanomaterials and Devices Laboratory, Department of Physics, University of Houston, Houston, Texas 77204, USA

[¥]Department of Electrical and Computer Engineering, University of Houston, Houston, Texas 77004, USA

[⊥]Energy Safety Research Institute, Swansea University Bay Campus, Swansea SA1 8EN, UK

*E-Mail (A. J. Wang): awang8@uh.edu

KEYWORDS: polymer nanocomposites, glass transitions, electronic switching, multiwall carbon nanotubes, human-body temperatures, wearable sensors, temperature coefficient of resistance

ABSTRACT

Nanocarbon-based disordered, conductive, polymeric nanocomposite materials (DCPNs) are increasingly being adopted in applications across the breadth of materials science. DCPNs characteristically exhibit poor electroconductive properties and irreproducibility/irreversibility in electronic phenomena, due largely to the percolative disordered nature intrinsic to such systems. The authors herein present an alternative approach towards enhancing the thermoresponsivity, repeatability, and reversibility of nanocarbon-based DCPNs in thermometric applications. This is empirically demonstrated using poly(octadecyl acrylate)-*grafted*-multiwall carbon nanotubes (PODA-*g*-MWCNTs) synthesized *via* reversible addition-fragmentation chain-transfer (RAFT) polymerization. Synthesized PODA-*g*-MWCNTs exhibit, repeatable, near-pyrexia sensitized, switch-like electronic responses across subtle glass transitions characterized by exceptionally large positive temperature coefficient of resistance values of 7,496.53 % K^{-1} $\pm$ 3,950.58 % K^{-1} at 315.1 K (42.0 °C). This corresponds to a sizable transition rate of 17.39 kΩ K^{-1} $\pm$ 0.49 kΩ K^{-1}, and recoverable near room temperature resistance values of 246.17 Ω $\pm$ 12.19 Ω at 298.2 K (25.1 °C). Near-human body temperature sensitized PODA-*g*-MWCNTs assembled in this work are promising candidates for wearable temperature sensors and other thermometric applications.

INTRODUCTION

Seminal work[1-2] on conjugated, disordered, conductive, polymeric nanocomposite materials has burgeoned into myriad interdisciplinary applications and technologies - spanning the gamut from advanced T-cell therapy nanomedicines[3] to state-of-the-art stretchable electronics (*e.g.*, printable conductive inks,[4] flexible LED displays,[5] and wearable electronic devices/skins[6]). The allure surrounding such materials principally stems from their functional tailorability across a breadth of physical, chemical, and physicochemical applications.[7-10] Whereas the notion of heterogeneous nanocomposite systems has long existed, utilitarian applications of disordered, conductive, polymeric nanocomposite materials (DCPNs) are of nascent interest, owing largely to their facile ease-of-processability, scalable manufacturing potential, mechanical/rheological properties in application, and comparatively low materials costs.[11] In sensing applications, nanocomposite materials are designed and nanoengineered to utilize both the functional properties of the individual components comprising the bulk structure as well as their interfacial interactions, yielding physically observable signals that relay critical information pertinent to the system.

As temperature-sensing/thermometric materials, developmental applications of DCPNs include flexible self-healing thermal sensors,[12] thermal runaway management materials in battery safety technologies,[13-14] thermoresponsive transient electronic systems,[15-16] and implantable *in vivo* multi-point temperature sensing devices.[17] Recent salient composite system designs/architectures exploiting phase transition phenomena[18-20] centered around temperature-dependent dimensional expansion and conductivity breakdown effects, elucidate the overarching mechanisms-of-action that render this group of materials unique. As a corollary to the eclecticism in the tailorability aspect of nanocomposite assembly, temperature sensors/switches sensitized to more practical temperature ranges (293 – 323 K (20 – 50 °C)) unattainable by functionally

analogous state-of-the-art inorganic oxides (*e.g.*, VO_2) have been realized.[21-22] Syntheses and characterization of thermometric polymeric micro-/nano-composite materials sensitized to near-room and human body temperatures have been achieved through synergistic schemes implementing solid-liquid phase transitions of hexadecane/octadecylamine-functionalized multiwall carbon nanotube (MWCNT) composites[22] and poly(ethylene) – poly(ethylene oxide) binary polymer/Ni-microparticle composites,[23] respectively. Alternative schemes implementing chlorinated poly(propylene carbonate)/carbon black composite foams have been proposed that exhibit switch-like electronic behavior (negative temperature coefficient of resistance (NTC) effect) near 313 K (40 °C), facilitated through heat-induced volumetric expansion of gaseous cavities permeating the composite foam.[24]

While research quantitatively delineating the dynamic physical interplays governing such conductive phase-change composite materials is still very much in its infancy, the bulk of significant empirical progress made in recent years in exploring the electronic/thermal properties of such systems report on sensitive temperature ranges >373 K (100 °C).[25-26] Little attention outside the references cited in this work is afforded to the development of human body temperature-sensitized thermistor-type diagnostic/monitoring materials for cost-effective biomedical applications. Such materials would serve as an excellent platform upon which to tailor cost-effective normothermia- (*i.e.*, normal human body temperatures (309.7 – 310.7 K (36.5 – 37.5 °C)))[27] or hyperpyrexia- (*i.e.*, fever corresponding to human body core temperatures >314 K (41.0 °C))[28] sensitized wearable diagnostic devices; particularly, for applications in impoverished or remote regions where obtaining/maintaining conventional temperature monitoring/diagnostic technologies is often cost-prohibitive or, alternatively, as cost-effective disposable pediatric or adult fever-monitoring devices for in-home use.

The notable high-accuracies of resistance temperature devices (RTDs), semiconductor temperature sensors, and thermocouples are contingent, respectively, on the repeatable resistance-temperature (*R*-*T*) relations that vary linearly in accordance with the Callender-Van Dusen equation,[29] linear *R*-*T* relations governed by bipolar junction transistor relations,[30] and changes in electric potential across thermojunctions induced *via* the Seebeck effect.[30] Irrespective of the accuracy, wide temperature sensing ranges (33 – 1,023 K),[31] and low-drift characteristics of high-performance RTDs, state-of-the-art Pt- or Cu-based RTD materials exhibit maximum empirical temperature coefficient of resistance (Π) values of 0.385 % K^{-1} and 0.658 % K^{-1}, respectively.[32] Similarly, thermocouple- and semiconductor-based temperature sensors with typical operational temperature ranges of 89 – 2573 K and 223 – 423 K, respectively, exhibit meager electronic responses to temperature fluctuations, typically in the tens of millivolts range.[33] As such, RTDs, thermocouple-, and semiconductor-based devices typically stipulate high-performance circuitry and signal conditioning components to augment/amplify sensitivities, where lead-wire contact resistances at thermojunctions can generate potentials comparable in size to generated signals. Thermocouples further stipulate the need for cold-junction compensation techniques to maintain isothermal conditions across all thermojunctions in circuit with thermoelectric measuring junctions.[34] Requisition of these additional electronic components increases design intricacies and is to the detriment of the cost-to-manufacture. Contrastingly, the high sensitivities of thermistor-type materials are a derivative of the nonlinearity in their temperature dependent resistance. As such, thermistor-type materials ordinarily exhibit a positive and/or negative Π effect near some critical temperature that corresponds to nonlinear, often sharp, changes in bulk electrical resistance. Π can be expressed as

$$\Pi = \frac{1}{R_o}\left(\frac{dR}{dT}\right), \quad (1)$$

where R_o, T, and R are the initial resistance of the material at some initial temperature T_o, the temperature of the material, and the resistance of the material at some temperature T, respectively.

Notwithstanding their exceptional tailorability, DCPNs are often marred by poor device performance and reproducibility within sensitive temperature ranges due fundamentally to the percolative electronic/phononic structure intrinsic to such systems.[35-36] In particular, nanocarbon-based DCPNs in thermometric applications correspondingly exhibit comparatively low electroconductive properties, at notably high nanocarbon-loadings, with representative near room temperature values of ~10^{-3} S cm^{-1} at 290 K (octadecylamine-functionalized MWCNT/hexadecane composites),[22] ~20 kΩ at 293 K (20 wt.% carboxylic acid-functionalized SWCNT/amide-functional fatty polybasic acid composites),[12] and ~10^{-3} S cm^{-1} at 298 K (25 wt.% graphite microparticle/octadecyl acrylate copolymer composites),[17] below each systems' respective melting temperature T_m. Worse yet, the vast majority of state-of-the-art human temperature-sensitized nanocarbon-based DCPNs implement solid-liquid phase transitions to effectuate reversible transient shifts from an already poorly conducting state to an insulating one in the Anderson localized sense. Such phase transition phenomena, while alluring from an electro-/thermo-responsivity perspective, impose significant device engineering challenges, requiring additional components to mitigate leakage of the active material in the liquid state and accommodate volumetric expansion effects.

The electronic and thermal responsivities of DCPN temperature sensing materials are an inextricable function of the convoluted interaction(s) occurring at the filler/host-matrix interface/interphase. Consequently, controlling the structure of this interfacial region is paramount to attaining highly thermoresponsive, reproducible signals, particularly in heterogeneous amorphous systems. In this work, near hyperpyrexia-sensitized thermistor-type nanocomposites

of poly(octadecyl acrylate)-*grafted*-MWCNTs (PODA-*g*-MWCNTs) with exceptionally large, reversible, repeatable, switch-like electronic responses near 315.1 K (42.0 °C) are reported on. Syntheses of PODA-*g*-MWCNTs was achieved *via* reversible addition-fragmentation chain transfer (RAFT) polymerization of octadecyl acrylate (ODA) initiated along the exohedral surfaces of functionalized MWCNTs at C=S bond sites of covalently grafted dithioester moieties functioning as chain-transfer agents, using 2,2'-azobis(2-methylpropionitrile) (AIBN) as a free-radical initiator (Scheme 1, S1, S2, Supporting Information).[37-38] The mechanism and kinetics of RAFT polymerization (Scheme 1, S1), as it pertains to the present study, can be partitioned into 6 distinct phases – namely, *Synthesis of RAFT Agents*, *Initiation/Propagation*, *Pre-Equilibrium*, *Re-Initiation*, *Primary Equilibrium*, and *Termination*.[39] The syntheses[40-41] of dithioester moieties from alcohols, carboxylic acids, and thiolocarboxylic esters and their use as intermediate chain-transfer agents[37-38, 42] in subsequent living polymerization reactions are well-documented.

Mechanistically, in contrast to first-order solid-liquid phase transitions, the PODA-*g*-MWCNTs synthesized in this work synergistically amplify subtle segmental conformational rearrangements of grafted PODA moieties along the exohedral surfaces of functionalized MWCNTs, occurring across the second-order glass transition temperature range ΔT_g of the system below T_m, where first- and second-order phase transitions here denote discontinuities in the 1st and 2nd derivatives of the associated Gibbs free energy, respectively. Homo- and copolymers of PODA are well-researched materials with the distinguishing propensity to form self-assembled 'crystalline' states below the melting point (~323 K), irrespective of the tacticity of the primary polymer backbone, *via* collective inter-sidechain van der Waals interactions between densely packed/aligned alkyl sidechain moieties, primarily in the *trans* configuration.[43-44] In addition to their remarkable aspect ratios, intrinsic thermal conductivities as high as 3,000 W m^{-1} K^{-1},[45-46] and

dynamic heat transfer applications,[45-46] MWCNTs were congruently selected as an optimal nanofiller candidate in consideration of their highly nonpolar exohedral surfaces conducive to enhancements in conformational interfacial interactions with covalently grafted PODA *via* long-range van der Waals forces.

The overarching objective of the present work is the communication of an alternative approach towards improving the repeatability/reversibility, electrical/thermal conductance, and thermoresponsivity of nanocarbon-based thermistor-type DCPNs near human body temperatures. This is achieved through tailored covalent modification of the filler/host-matrix interface/interphase and effectuated *via* form-stable 2nd-order glass transitions. Application of the PODA-*g*-MWCNTs synthesized in this work as a potential candidate for human body temperature sensitized wearable temperature sensors is demonstrated.

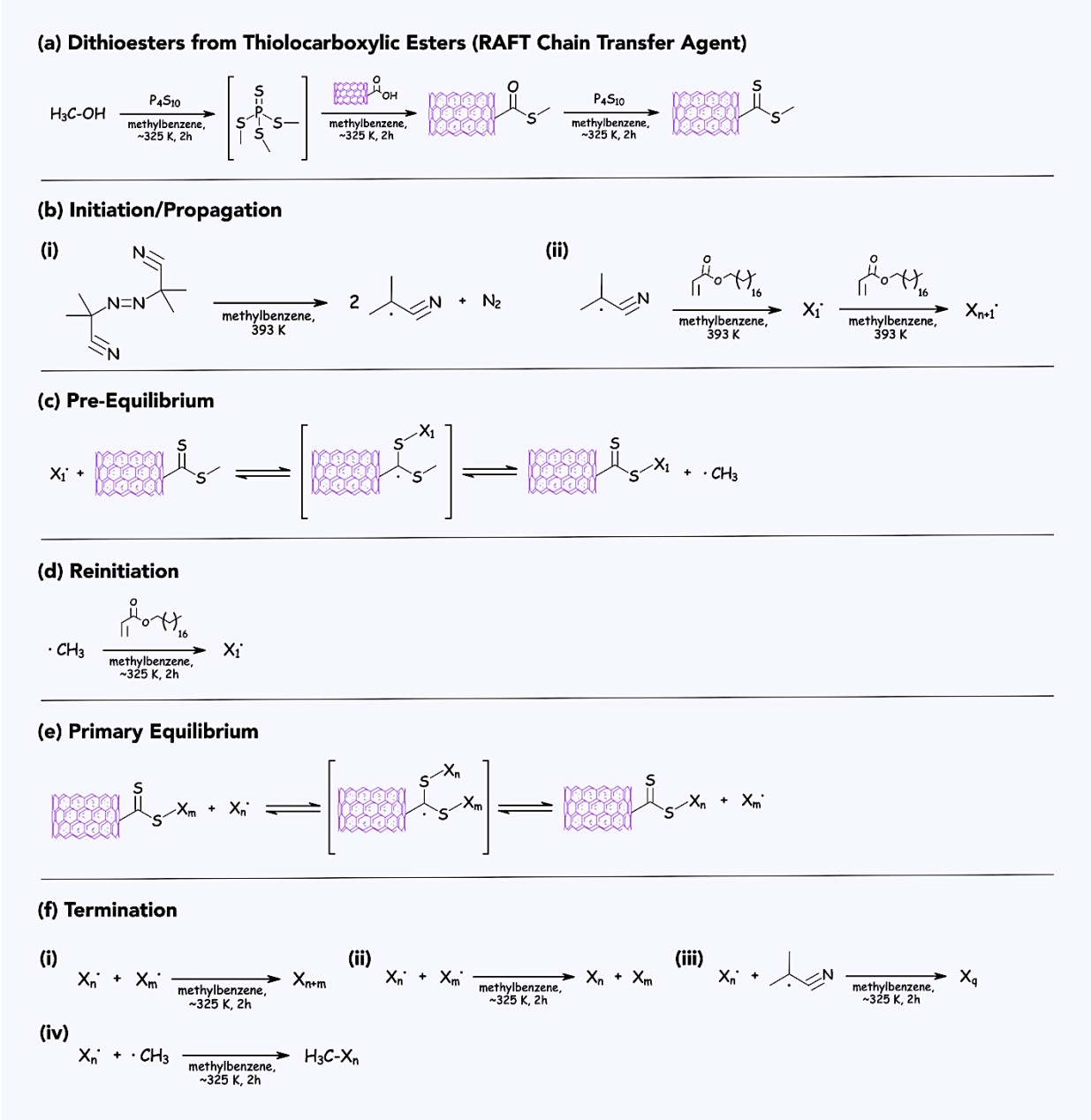

Scheme 1. Synthesis of PODA-*g*-MWCNTs via RAFT-Polymerization. (a) Synthesis of RAFT chain-transfer agents comprised of dithioester moieties from thiolocarboxylic esters in the presence of Berzelius reagent P_4S_{10} subsequent to reactions between an intermediate product of MeOH and P_4S_{10} and carboxylic acid moieties. (b) The RAFT process (i) initiates with the decomposition of AIBN into free radical species and N_2; (ii) propagation proceeds through subsequent reactions between evolved free radical species and monomeric ODA to yield intermediate radical oligomeric units $X_1^{\bullet}$, which undergo further addition reactions with ODA to yield propagating radical oligomeric units $X_{n+1}^{\bullet}$. (c) The pre-equilibrium phase, where reactive nucleophilic C = S bonds of dithioester moieties undergo reversible radical addition reactions with $X_1^{\bullet}$ to form intermediate MWCNT-immobilized adduct radical species that can fragment into polymeric chain-transfer agents and a free radical ($\bullet CH_3$). (d) The reinitiation phase proceeds via

further radical addition reactions with monomeric ODA, shifting the *Pre-Equilibrium* phase towards the right side of (c). (e) RAFT polymerization is critically dependent on the *Primary-Equilibrium* phase, where cascading equilibration reactions between remaining propagating radicals ($X_n^{\bullet}$ and $X_m^{\bullet}$) and unterminated RAFT agents favor reaction products with a narrow polydispersity index. (f) The RAFT process ends with *Termination* via disproportionation (inter-radical H-transfer) and/or combination (inter-radical coupling) schemes – a non-exhaustive set of possible termination reactions are presented in (i-iv).

RESULTS AND DISCUSSION

AFM-IR Absorbance and Electron Microscopy Analyses of PODA-*g*-MWCNTs. Direct IR absorbance spectra of neat PODA (F80) and 2.57 wt.% PODA-*g*-MWCNT (F83) samples, obtained *via* an integrated AFM – infrared spectroscopy (AFM-IR) technique with nano-lateral resolution, are presented along with corresponding 3D orthographic-projection AFM topography micrographs in Figure 1. The topography of neat PODA resembles a network of highly entangled strands ~1 – 2 μm in diameter (Figure 1a), typical of poly(alkyl acrylates).[44] Figure 1b provides a higher magnification topography micrograph of F83 at a cluster of intersecting conductive conduits of PODA-*g*-MWCNTs. Imparting structural order *via* synergistic covalent interactions and their derivative effects between MWCNTs and grafted PODA moieties can improve interfacial heat transfer between covalently linked MWCNTs and PODA by diffusion of thermal energy and/or phononic coupling effects through higher-frequency non-propagating/localized vibrational modes – whereas, with increasing disorder, phonon states generally tend towards Anderson localized excitations.[47]

IR-spectra were collected at target-specific locations across respective sample surfaces to investigate uniformity and variations in functional group species and distribution between F80 (Figure 1c) and F83 (Figure 1d). Four prominent characteristic IR-absorbance peaks of F80 (Figure 1c) at 1783 cm^{-1} (C=O stretching),[48] 1466 cm^{-1} (-CH_2- scissoring),[48] 1258 cm^{-1} (-CH_2-scissoring),[48] and 1170 cm^{-1} (C-O-C valence vibrations/C-O stretching)[9] verify polymerization of ODA into PODA. Three characteristic IR-absorbance bands observed in the IR-spectra of F83 (Figure 1d) not present in the IR-spectra of F80 at 1585 cm^{-1} (sp^2 carbon),[48] 1351 cm^{-1} (sp^3 carbon),[49] and 1040 cm^{-1} (C=S stretching)[50] confirm the presence of thioester-/dithioester-

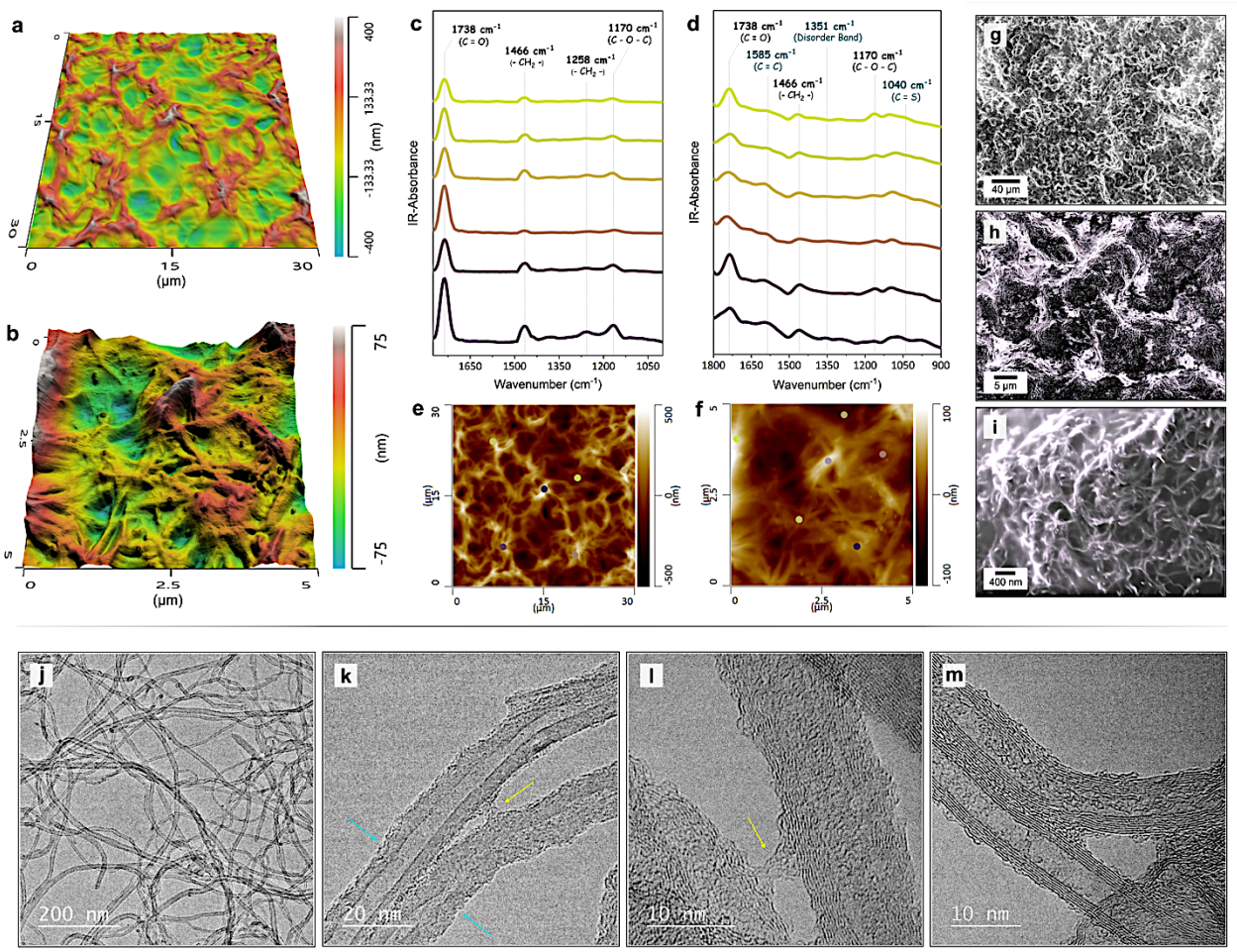

Figure 1. False-color 3D AFM topography orthographic projection micrographs of (a) F80 and (b) F83. Direct IR absorbance spectra of (c) F80 and (d) F83. AFM topography micrographs of (e) F80 and (f) F83 with overlaid color-coordinated dot markers corresponding to (c,d), respectively. (g-i) Field-emission scanning electron micrographs of F83 at varying magnifications. (j-m) Field-emission transmission electron microscopy micrographs of F83 at varying magnifications (Note: blue arrows denote regions of observed constriction and yellow arrows denote regions of PODA-bridged T-MWCNTs).

functionalized MWCNTs. The colored markers superimposed on the AFM topography micrographs of F80 (Figure 1e) and F83 (Figure 1f) corresponding to Figure 1c,d, respectively, denote where IR-spectra were measured on the sample surface. Corresponding FE-SEM micrographs depicting the microstructure of the surface of F83 are presented in Figure 1g-i. The more conductive interior cores of the dendritic conduits presented in Figure 1b are resolved as a

system of highly interconnected PODA-*g*-MWCNTs, as illustrated in Figure 1i, where the intrinsically large aspect ratios of the MWCNTs are evidently preserved. It is critical to note that large aspect ratios are vital to preserving the intrinsic conductivities of the MWCNTs and in minimizing R_c by increasing the number of direct-charge tunneling junctions per MWCNT. From a congruent phononic perspective, shorter nanotubes have been shown to exhibit phononic transitions, where the lowest frequency phonon modes are upshifted to higher frequencies, resulting in weaker phononic coupling with the host polymer matrix.[45] Weaker phonon coupling exists in shorter nanotube-based polymeric composite systems because energy transported in higher-frequency phonons must first undergo inter-phonon coupling in order to transfer the energy to lower- frequency phonon modes, before energy can be transferred to the polymer matrix. It has been conversely shown that covalent bonding with the polymer matrix can result in strong coupling *via* higher frequency phonon modes, which is a viable route towards enhancing phononic coupling between a nanofiller and its host polymer matrix.[45]

Concordantly, in this work, free-radical polymerization of ODA onto and between MWCNTs, using functionally introduced thioester/dithioester linkages as chain transfer agents, facilitates close-proximity covalent bonding between the conjugated nanostructures and the primary acrylate backbone. Controlling the dimensionality of this linker-region has been shown to play a critical role in maximizing interchain thermal conductance, where short-chain, low molecular weight linkers are the epitome.[51] Transmission electron microscopy (TEM) micrographs (Figure 1j-m) of F83 corroborate high aspect ratios and resolve the nanostructure of F83 as a system of tightly PODA-wrapped T-MWCNTs. Observed regions of PODA-bridged T-MWCNTs spanning ~5 nm across (Figure 1k,l) strongly support the syntheses techniques adopted in this work. Regions where tightly-wrapped PODA is observed constricting the outer walls of T-

MWCNTs are demarcated by blue arrows (Figure 1k), indicative of a high degree of proximal conformity across the T-MWCNT/PODA interface/interphase. Figure 1j demonstrates long-range PODA-wrapping, a common feature observed in F83. Such long-range order is conducive to a larger number of internanotube tunneling junctions with a strong dependency on the conformational arrangement of chemisorbed/physisorbed PODA moieties. A high-resolution TEM (HRTEM) micrograph of F83 (Figure 1m) clearly contrasts and resolves the T-MWCNT/PODA interface, where a high degree of exohedral conformity is observed in grafted PODA moieties.

Spectroscopic Analyses of PODA-*g*-MWCNTs. Heat transport in amorphous solids is facilitated through dynamic phononic and electronic contributions and interactions. While a consensus regarding holistic phonon transport mechanisms in amorphous composite materials remains contentious, covalent bridging across the filler/host-matrix interface is critical towards realizing homogeneous phonon propagation (*i.e.*, optimized interfacial thermal conductance) across the heterogenous domains comprising the bulk structure.[51-52] XPS spectra obtained as evidence for C-S and/or C=S bond formation, requisite moieties of thioester and dithioester functional groups, respectively, are presented along with supporting Raman and IR absorbance spectra and a schematic illustration of thioester-/dithioester-functionalized nanotubes in Figure 2. XPS spectra of T-MWCNTs (Figure 2a) reveal two distinct binding energy regimes at 162 – 172 eV and 230 – 235 eV, characteristic of S *2s* and S *2p* electron configurations, respectively, not present in the offset spectra of pristine MWCNTs (P-MWCNTs). Deconvoluted S *2p* and S *2s* binding energy regimes between 162 – 172 eV (Figure 2b) and 224 – 236 eV (Figure 2c), respectively, are resolved as characteristic peaks centered at 164.8 eV (thioester/dithioester),[53] 170.3 eV (C-S-CH_3),[54] 227.5 eV (C-S),[49] and 231.6 eV (C-S-C)[55] and corroborate the formation of thioester/dithioester moieties. Comparing the XPS spectra of P-MWCNTs and T-MWCNTs

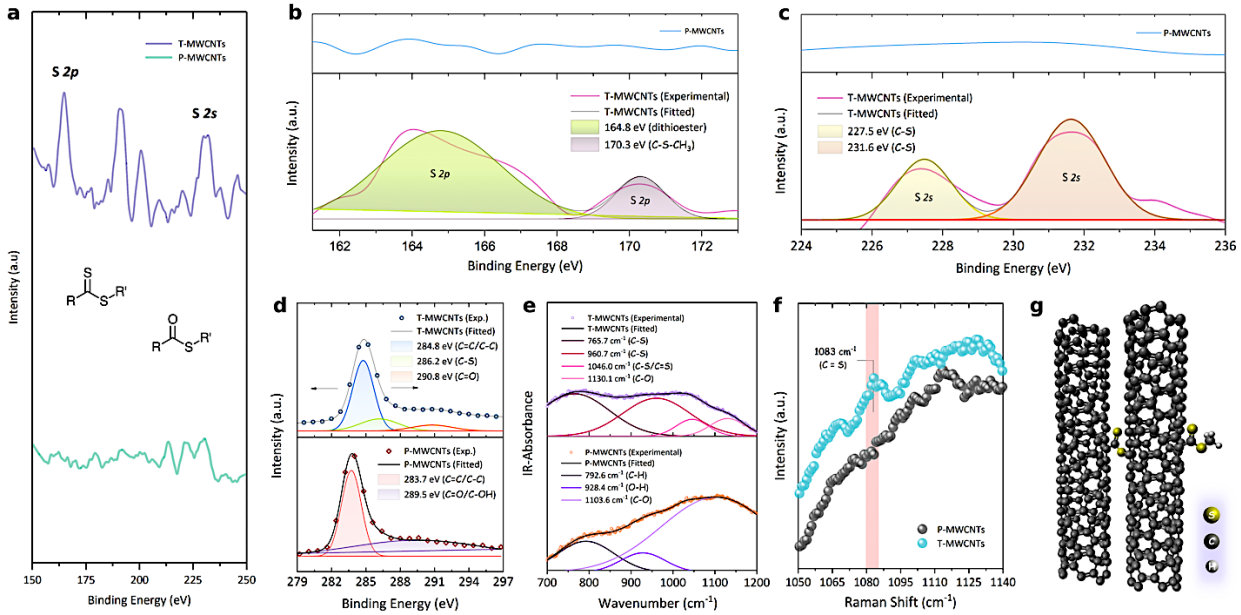

Figure 2. (a-d) XPS spectra of P-MWCNTs and T-MWCNTs from (a) 150-250 eV, (b) 162-172 eV, (c) 224-236 eV, and (d) 279-297 eV. The 2 inset chemical structures in (a) are dithioester and thioester functional groups, where R and R' are MWCNT and PODA/methyl moieties, respectively. The top-stacked spectra in (b,c) are the corresponding electron count spectra of P-MWCNTs taken across the same binding energy and intensity intervals. (e) FTIR spectra of T-MWCNTs (top) and P-MWCNTs (bottom). (f) Raman spectra of P-MWCNTs and T-MWCNTs. (g) A schematic illustration of dithioester-grafted/-functionalized MWCNTs.

(Figure 2d) across the 279-297 eV regime (C *1s* binding energies), a characteristic peak at 286.2 eV (C-S)[56] leads to broadening of the C *1s* band. It should be noted that the fitted peaks in Figure 2b,c were not force-fitted to further deconvolute the experimental spectra as XPS data obtained across the S *2p* and S *2s* core-level binding energies are from broad as opposed to high-resolution scans calibrated to the C *1s* regime and are presented to corroborate complementary vibrational and Raman spectra (Figure S1, Supporting Information).

FT-IR absorbance spectra of P-MWCNTs and T-MWCNTs (Figure 2e) reveal several new peaks centered at 757.7 cm^{-1} (C-S),[50] 960.7 cm^{-1} (C-S),[50] and 1046.0 cm^{-1} (C-S/C=S)[50] for T-MWCNTs not present in IR-spectra of P-MWCNTs. Complementary Raman spectra of T-

MWCNTs (Figure 2f) exhibit a characteristic peak at 1083 cm^{-1} (C=S)[38, 57] absent in the corresponding spectra of P-MWCNTs, with additional signature peaks between 660 – 770 cm^{-1} strongly supporting the existence of dithioester groups (Figure S2, Supporting Information). A schematic illustration of dithioester-grafted/-functionalized nanotubes is provided in Figure 2g. Additional Raman, direct IR-absorbance, and XPS spectra of F80, F83, and 4.81 wt.% PODA-*g*-MWCNT (F86) samples are found in the *Supporting Information* (Figure S3, Supporting Information).

Thermal Conductivity Mapping *via* AFM-Scanning Thermal Microscopy. The thermal conductivity of F83 was indirectly quantitatively mapped using an integrated AFM-scanning thermal microscopy (SThM) technique at 313 K and 353 K, as presented in Figure 3a and Figure 3b, respectively. Here, changes in electric potential across a Thermalever™ AFM nanometric probe tip (<30 nm), arranged in a Wheatstone bridge configuration, denote regions of varying temperature in response to applied heat, which is used to distinguish regions of differing thermal conductivity with nano-lateral resolution. Areas of higher positive potential (demarcated in yellow) denote regions of higher thermal conductivity while areas of larger negative potential (demarcated in blue) denote regions of lower thermal conductivity. From Figure 3a, large-scale electronic and thermal connectivity across F83 is observed, where the topology closely resembles interconnected, dendritic, tubular, conduits ranging in diameter between ~100 – 300 nm. Above T_m, F83 behaves as a form-stable, viscous conductive paraffinic fluid with seemingly isolated regions that exhibit larger thermal conductivities than those observed in F83 for $T < T_c$, consistent with amorphous behavior.[51] Minor volumetric swelling of F83 from 313 K to 353 K is observed in height profiles from matching AFM topography micrographs (Figure S4, Supporting Information).

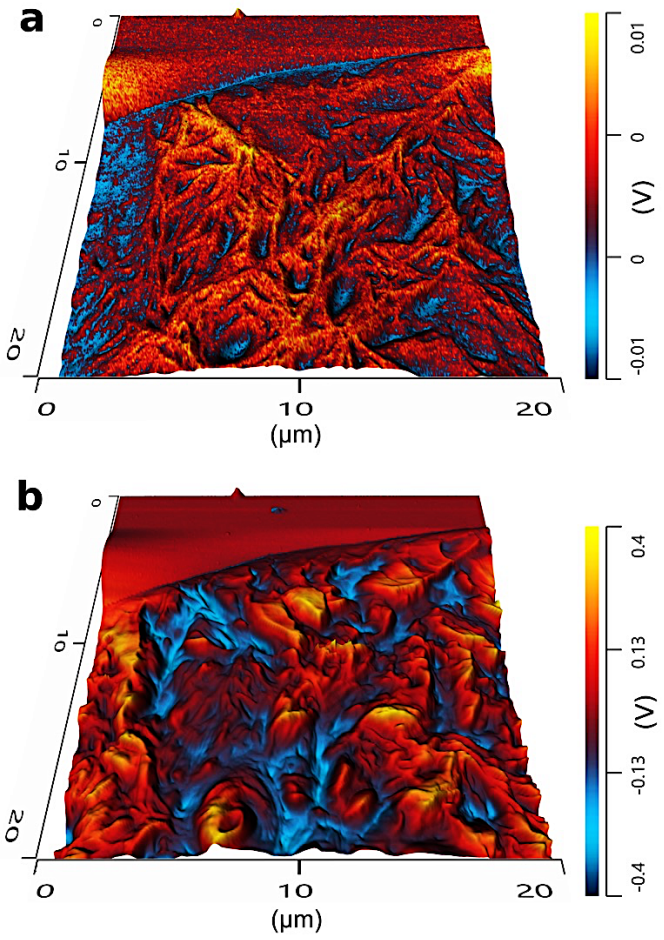

Figure 3. False-color thermal conductivity mapping overlays on 3D AFM topography orthographic projection micrographs of an ~400 μm^2 area of F83 at (a) 313 K and (b) 353 K.

Differential Thermal Analysis and Glass Transition Ranges of PODA-*g*-MWCNTs. Differential thermal analysis was used to corroborate and gain further insight on the large Π responses of the PODA-*g*-MWCNTs assembled in this work. From the DSC thermograms presented in Figure 4a, a contrasting reduction in the change in enthalpy ΔH of F83 in comparison to neat PODA (F80) is immediately apparent. Magnifications of the heatflow curves in Figure 4a are presented in Figure 4b (F80) and Figure 4c (F83) with melting temperatures of $T_{m_{\mathrm{F80}}}$= 324.18 K and $T_{m_{\mathrm{F83}}}$= 326.69 K, respectively, where a distinct trend in increasing T_m with increasing

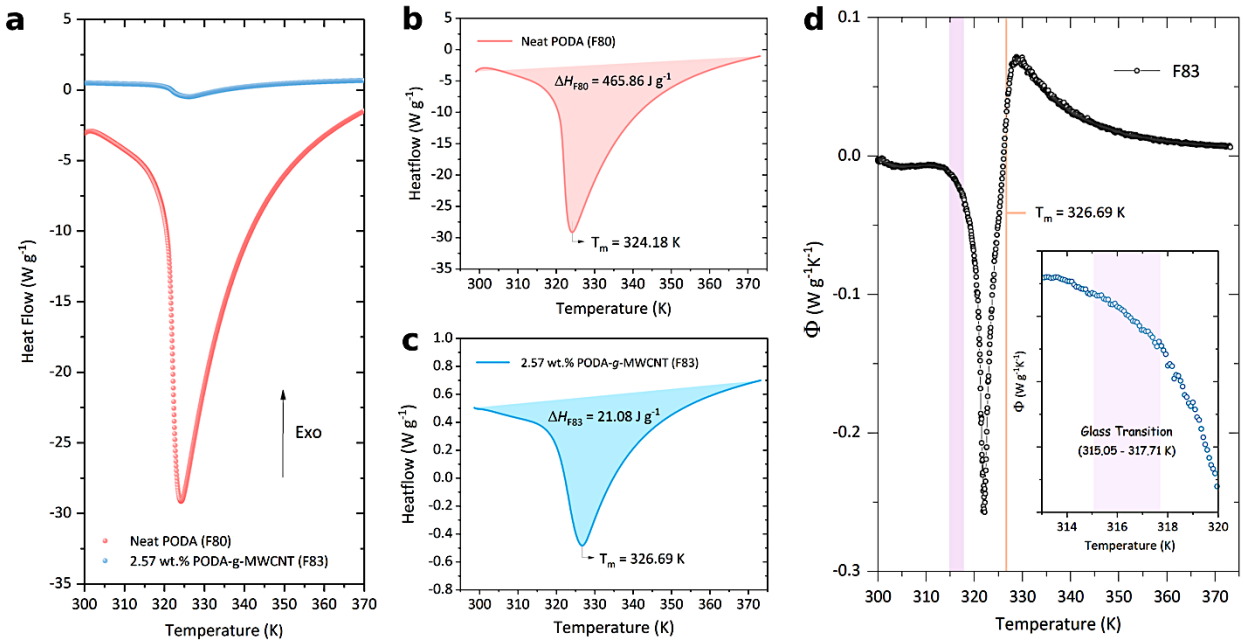

Figure 4. (a) DSC thermograms of F80 and F83. Heat flow curves highlighting ΔH and T_m for (b) F80 and (c) F83. d) The first derivative of (c) with respect to temperature near the glass transition range (315.08 – 317.71 K) – the inset is a magnification of the glass transition range ($\Delta T_{g_{F83}}$).

MWCNT concentration is observed (Figure S5, Supporting Information). This is attributed to a combined effect of higher MWCNT concentrations and the notion of increasing M_w of RAFT-polymerized ODA with increasing concentration of initial RAFT agent.[41] More intriguing is that while F80 exhibits a change in enthalpy of ΔH_{F80} = 465.86 J g^{-1}, F83 and F86 exhibit strikingly smaller values of ΔH_{F83} = 21.08 J g^{-1} and ΔH_{F86} = 38.96 J g^{-1} (Figure S5, Supporting Information), respectively. Recall from the 1st law of thermodynamics, under isobaric conditions, state variable ΔH reduces to $\Delta H = Q$, where Q is heat absorbed by the system - the marked reduction in heat energy per unit mass required to initiate 1st and 2nd order phase transitions correspondingly increase the sensitivity and responsivity of F83 and F86 in comparison to F80. The first derivative of Figure 4c is plotted (Figure 4d) to elucidate $\Delta T_{g_{F83}}$, where the inset is a magnification of the $\Delta T_{g_{F83}}$ region existing between 315.08 – 317.71 K. Reductions in ΔH across $\Delta T_{g_{F83}}$ directly imply proportional

reductions in specific heat under isobaric conditions as the MWCNT-grafted PODA moieties transition from a self-entangled state, to one where the primary acrylate backbones are dynamically extended/unraveled with increasing degrees of freedom.[58] TGA thermograms of F80, F83, and F86 corroborate the MWCNT-loadings of F83 and F86 and support the existence of chemisorbed functional groups (Table S1, Figure S6, Supporting Information).

***I-V* Characterization of PODA-*g*-MWCNTs.** Temperature dependent resistance values of 1.69 wt.% (F81), 2.57 wt.% (F83), 4.81 wt.% (F86), and 6.22 wt.% (F87) PODA-*g*-MWCNT samples were measured at a temperature resolution of 1.0×10^{-3} K as described in the *Experimental Section* (Table S1, Figure S7, S8, and S9, Supporting Information). For all experimental samples, heating and cooling cycles between 300 – 330 K were conducted at mean linear heating and cooling rates of 7.45×10^{-3} K s^{-1} (0.45 K min^{-1}) and -3.65×10^{-3} K s^{-1} (-0.22 K min^{-1}), respectively, at standard ambient temperature, pressure, and relative-humidity (Figure S8, Supporting Information) unless specified otherwise. Relatively slow heating/cooling rates were selected to simulate rates of temperature shifts in human body temperature thermometric applications as well as to elucidate mechanisms-of-action. It should be noted that while the experimental cooling rate is approximated here by the slope of a linear-regression, the actual temperature decayed exponentially, as described in the *Supporting Information* (Figure S8b, Supporting Information). All samples were allowed to re-equilibrate to room temperature (~296 K) between consecutive thermal cycles.

As sample F83 exhibits DC electronic transport properties most conducive to realistic sensor-/switch-type device requirements (*i.e.*, practical electrical conductance values, large Π near sensing temperature(s), mechanical flexibility, and repeatability/reversibility of electronic phenomena) amongst the nanomaterials synthesized in this work, this portion of the results is

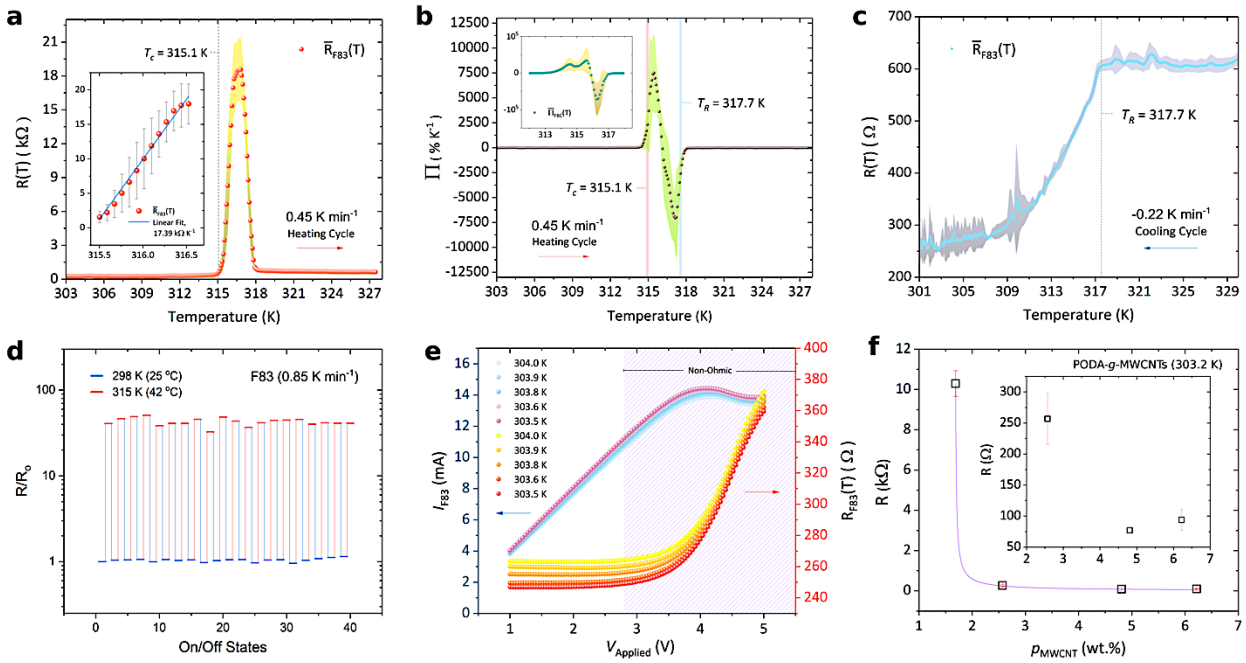

Figure 5. (a) Temperature-dependent resistance of sample F83 near T_c = 315.1 K and T_R = 317.7 K during heating cycles. (b) Temperature coefficient of resistance (Π) of sample F83 near T_c and T_R (Inset: Π of control group sample F8C near T_c). (c) Temperature-dependent resistance of F83 across cooling cycles from 330 – 300 K. (Note: the shaded areas in (a-c) denote associated error). (d) On/Off states during consecutive heating/cooling transitions between 298 K and 315 K, respectively, at a heating rate of 0.85 K min^{-1} for 40 transitions. (e) Voltage-dependent current (I_{F83}) and resistance (R_{F83}) at 304.0 K, 303.9 K, 303.8 K, 303.6 K, and 303.5 K. (f) Near room temperature resistance values as a function of T-MWCNT concentration (Inset: magnification of F83, F86, and F87).

communicated with principle emphasis on F83. F83 notably transitions more abruptly across a narrower temperature range with exceptionally small associated uncertainty values, while also exhibiting an ideal balance between cost-effective nanotube loading and practical RT resistance values in comparison to all other samples synthesized in this work. This is reasoned to result from an optimizable synergetic effect between thioester-/dithioester-functionalized MWCNTs (T-MWCNTs) and grafted PODA moieties with a dependence on the respective concentration of T-MWCNTs with respect to ODA derivatives.

Below a critical transition temperature $T_{C_{F83}}$ during heating cycles, F83 retains its comparatively low electrical resistance values between 300 K (241.77 Ω ± 16.48 Ω) to 313 K (312.60 Ω ± 18.47 Ω) (Figure S10a, Supporting Information). In reference to Figure 5a, F83 abruptly transitions from a conductive (1,554.31 ± 829.20 Ω at 315.5 K) towards near-insulating state (17,968.93 Ω ± 2,886.47 Ω at 316.5 K) across the span of 1.0 K near a critical temperature ($T_{C_{F83}}$ = 315.1 K), corresponding to an unusually sizable, repeatable rate of increase in resistance (17,386.28 Ω K^{-1} ± 492.25 Ω K^{-1}) across this narrow range (inset of Figure 5a). This is subsequently followed by a near-symmetrically sharp recovery of conductance at a temperature T_R = 317.0 K from 18,057.07 Ω ± 2,461.93 Ω to 787.74 Ω ± 27.73 Ω (318.4 K) (Figure S10b, Supporting Information). Remarkably, as F83 is heated further through its melting temperature $T_{m_{F83}}$ = 326.69 K, no appreciable change in resistance is observed, indicating that no further appreciable change in electronic structure occurs across T_m in comparison to that associated with $\Delta T_{g_{F83}}$ (Figure S10c, Supporting Information). This nearly symmetrical recovery of conductance is further demonstrated by the Π plot of F83 (Π_{F83}) presented in Figure 5b, where the repeatable thermoresponsiveness of F83 is evident through the exceptionally large, inversely-mirroring mean extrema in Π_{F83} of 7,496.53 % K^{-1} ± 3,950.58 % K^{-1} and -7,046.34 % K^{-1} ± 3,323.46 % K^{-1}, measured at 315.1K and 317.7 K, respectively. The Π of a control group comprised of 2.57 wt.% T-MWCNTs in neat PODA (F8C) is presented in the inset of Figure 5b to highlight the significance of the critical chemical functionalization techniques implemented in this work (Schemes 1, 2). F8C characteristically exhibits large desultory Π responses between 302 – 305 K, which are attributed to random, transient, recoverable loss of electronic transport pathways (Figure S11, Supporting Information).

While F8C does exhibit irregular electronic responses near the critical temperature of F83 ($T_{C_{F83}}$ = 315.1 K), the resistance across F8C plotted as a function of temperature across 5 heating/cooling cycles plainly communicate the irregular unalluring resistance values measured for F8C (Figure S12, Supporting Information). F83 initiates exponential recovery of conductance with astonishing accuracy at the same T_R = 317.7 K observed in heating cycles while transitioning back to an amorphous vitreous state - ultimately recovering its initial resistance at room temperature (246.17 Ω ± 12.19 Ω at 298.2 K) (Figure 5c). The sharp recovery of conductance above T_R upon further heating is attributed to the abrupt physical/conformational deformation across the PODA-MWCNT interface/interphase corresponding to the glass transition range that disrupts the net number of electron tunneling junctions, which are somewhat recovered after the initial transitional shockwave. Beyond T_R, as F83 approaches T_m, the dynamic motions of covalently grafted alkyacrylate moieties no longer seem to perturb the electronic structure to the extent observed across the glass transition range. It should be noted that the small observed fluctuations in resistance across cooling cycles (Figure 5c) between ~310 – 300 K may be partly/wholly attributed to the minor shift in contact resistance resulting from subtle contact shifts between the PtIr needle-tip electrodes and the thin-film Au electrodes used for electronic characterization (Figure S9, Supporting Information).

F83 exhibits relatively small changes in resistance across cooling cycles within the range $T_R < T \leq T_m$ as the material slowly transitions from a viscous liquid to a more rigid elastomeric state, analogous to the electronic behavior observed while traversing the same temperature range during associated heating cycles (Figure S10d, Supporting Information). Stacked plots of R_{F83} and Π_{F8C} across each contiguous heating/cooling cycle corresponding to Figure 5a-c are presented in the *Supporting Information* to emphasize the repeatability of the reversible electronic response

(Figure S13, Supporting Information). Switch-like behavior of F83 is emphasized by Figure 5d, where a semi-log plot of the normalized resistance across consecutive, repeatable, reversible transitions between ON (244.34 Ω ± 2.37 Ω)/OFF (10,043.52 Ω ± 222.40 Ω) states, for 40 contiguous ON/OFF transitions are shown at a faster heating rate of 0.85 K min^{-1}.

The *I-V* characteristics of F83 in response to higher applied fields are presented in Figure 5e for consecutive DC forward voltage sweeps from 1 – 5 V at near room temperature. It is important to note that the *I-V* characteristics of F83 remain Ohmic for low applied biases (<3.0 V). At higher applied biases (>3.0 V), the current through F83 tapers off in a manner inconsistent with Poole-Frenkel conduction, Schottky effect dominated conduction, or space-charge limited conduction (SCLC) mechanisms (Figure S14, Supporting Information).[59-60] At forward biases >3.0 V, regions of hybridized sp^3 orbitals formed from covalently bonded functional moieties and intrinsic defects on the exohedral surfaces of PODA-*g*-MWCNTs could potentially give rise to an increasing number of disordered topological energy trap states. Topological traps can result in a fermionic separation of charge carriers (*i.e.*, *fast* or *slow* carriers) that is augmented at higher applied electric fields.[61] Such charge carrier trap sites in coaction with self-trapping phenomena characterized by polaronic behavior can result in the peculiar decrease in current through F83 observed near an applied forward bias of ~4.0 V (Figure S14c, Supporting Information).

Fowler-Nordheim (FN) tunneling-type effects can be neglected here as the *I-V* behavior of F83 does not fit FN-type functions nor does F83 exhibit the characteristic negative slope and inflection point in plots of $\ln[IV^{-2}]$ as a function of V^{-1}.[62] It should be noted that the *I-V* behavior of F83 is representative of an amalgam of likely conduction mechanisms, where internanotube contact resistance, Joule heating, and diffusion current effects cannot be neglected. The temperature dependency and sensitivity of F83 is further highlighted in Figure 5e, where a distinct

trend of decreasing bulk resistance with decreasing temperature is shown. In comparison to F83, F87 (6.22 wt.% PODA-*g*- MWCNTs) carries a larger current accommodated by a larger carrier mobility (*i.e.*, higher concentration of sp^2-hybridized carbon) and exhibits markedly different *I-V* characteristics in comparison to F83 (Figure S15, Supporting Information). Two distinct Ohmic regions partitioned by a region between 2.5 – 3.5 V characterized by a sharp decrease in dI/dV, conceivably correspond to a critical activation potential beyond which charge trapping in oxygen-containing impurities along the conjugated structures can occur (Figure S16, Supporting Information).

While F81 (1.69 wt.% PODA-*g*-MWCNTs) does exhibit particularly large Π values on the order of 10^8 % K^{-1}, resulting from abrupt 9-order of magnitude spikes in resistance from 10^1 – 10^9 kΩ, the responses are irregular in comparison to those of F83. Such irregular responses coupled with large operational resistance values (10-60 kΩ) render F81 largely unsuitable for simple switch-/sensing-circuits – albeit F81 did exhibit notable repeatability in electronic states across cooling cycles and could find potential application as thermometric sensors in soft robotics (Figure S17, Supporting Information).[12] F86 (4.81 wt.% PODA-*g*-MWCNTs) uniquely exhibits a negative Π-dominant effect during heating cycles occurring as a corollary to the sharp recovery of conductance near its recovery temperature (Figure S18, Supporting Information). F87 exhibits comparatively small and irregular electronic responses near $T_{C_{F83}}$ in comparison to F83 (Figure S19, Supporting Information). The resistance values for F81, F83, F86, and F87 as a function of PODA-*g*-MWCNT concentration are presented in Figure 5f, where distinct percolative behavior is apparent when fitted with a Belehradek-type power function.

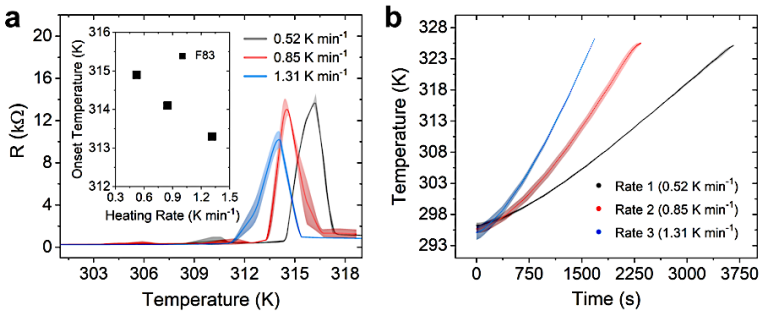

Figure 6. (a) Temperature dependent resistance of F83 at heating rates of 0.52 K min^{-1}, 0.85 K min^{-1}, and 1.31 K min^{-1} (Inset: onset temperature of resistance spike determined by the maximum of the first derivative of each R(T) curve). (b) Heating rates corresponding to (a) (Note: the shaded areas denote associated error).

The onset temperature of the resistance spike for F83 was observed to depend approximately linearly on the heating rate (Figure 6a). Corresponding heating rates of 0.52 K min^{-1}, 0.85 K min^{-1}, and 1.31 K min^{-1} are shown in Figure 6b, where averages of two consecutive heating cycles were used for each of the 3 heating rates (Figure 6a,b). The onset temperatures presented in the inset of Figure 6a were determined by the maxima of the first-derivatives of each respective R(T) curve. Maxima of R(T) curves presented in Figure 6a were not used directly for comparison as the density of datapoints near the critical transition temperature varies with heating/cooling rate because of the constant sampling rate. Shifting of onset temperature of conductivity breakdown with varying heating rates as presented in Figure 6a is an expected result as glass transitions are kinetic processes with a well-known dependency on heating/cooling rate.[63-64] Notably, the temperature dependent resistance response of F83 for each of the three heating rates was repeatable.

Glass Transition-Facilitated Reversible Electronic Switching in PODA-*g*-MWCNTs. It is important to note that glass transitions, dissimilar to 1st-order phase transitions, are complex, convoluted processes, classically described through either kinetic or equilibrium theoretical frameworks, and critically dependent on a number of physical, chemical, and physicochemical

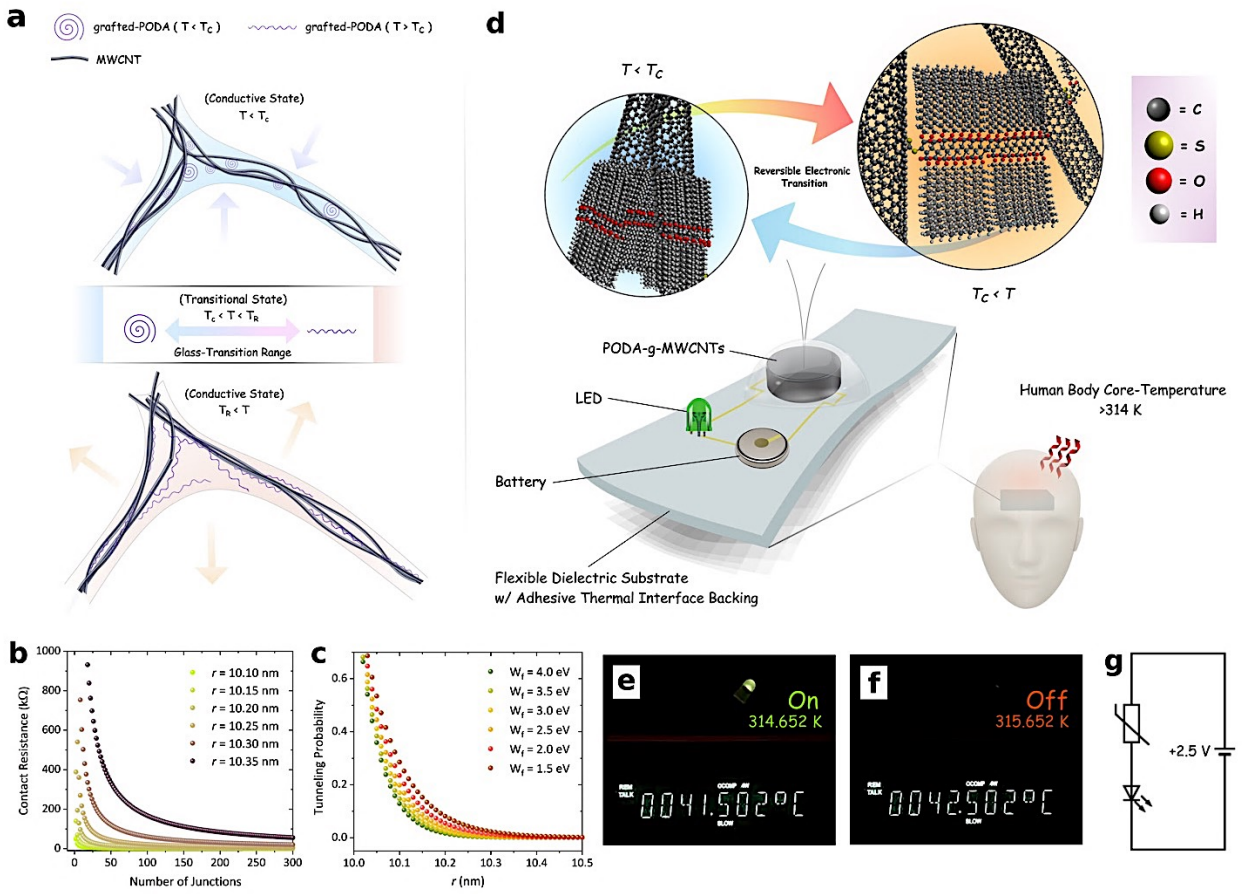

Figure 7. (a) Schematic cartoon illustrating the reversible, subtle conformational changes in grafted PODA moieties as it pertains to electronic switching inside bundles of intersecting PODA-*g*-MWCNT/PODA conduits for (top) $T < T_C$, (middle) $T_C < T < T_R$, and (bottom) $T_R < T$. (b) Internanotube contact resistance (R_c) as a function of the number of tunneling junctions for differing interaxial separation distances and (c) tunneling probability (τ) across internanotube tunneling junctions as a function of interaxial separation distance for differing potential barrier values. (d) Schematic cartoon depicting the reversible electronic transition and a potential biomedical application of F83 as a hyperpyrexia-sensitized thermometric sensor (Note: all components and their configurations/arrangements in (a,d) are not to scale and are intended only to convey the essence of principle). Digital photographs of the green LED circuit used to demonstrate (e) ON and (f) OFF states corresponding to the real-time temperature values illuminated on the front-panel display of a data acquisition system (Keithley 2700). (g) Circuit diagram used in (e,f).

parameters.[65-66] While a comprehensive canonical delineation of the underlying nature of glass transitions is still very much an active area of research in current polymer science, glass transition processes can generally be partitioned into 3 distinct sequential stages – namely, the gamma

transition (T_γ), beta transition (T_β), and glass transition (T_g).[65, 67] These transitional phases are instrumental in describing the large, repeatable, reversible electronic responses foremost to this work. At the onset of T_γ, as F83 approaches T_c, localized vibrational interbond bending and/or stretching and localized alkyl sidechain sectional movement results in the subtle nearly linear increase in resistance observed in heating cycles for $T < T_C$ (Figure S10a, Supporting Information). As the temperature is increased further, transitioning from T_γ to T_β, localized segmental alkyl sidechain motions extend to localized movements of entire alkyl sidechain moieties.[58] Upon reaching T_g, localized sidechain motions evolve to long-range coordinated movements of both the alkyl sidechains as well as their respective primary acrylate backbones, corresponding to large-scale orchestrated conformational/structural rearrangement at the PODA-MWCNT interface/interphase.[65-66] Such a conformational reorganization disrupts any initial predominating van der Waals interactions between alkyl sidechain moieties of both covalently grafted and physiosorbed PODA, as illustrated in Figure 7a, where the structural/conformational arrangement of grafted PODA moieties below and above T_c are depicted through the purple raveled and unraveled spirals, respectively. This reversible physical rearrangement across T_c causes an abrupt nanometric shift in internanotube contact, which can result in a dramatic increase in internanotube contact resistance (R_c) and exponential decrease in internanotube tunneling probability (τ) as reasoned within the Landauer-Büttiker formalism describing tunneling-assisted direct-charge transfer – herein, direct-charge transfer implies interaxial nanotube separation distances on the order of the van der Waals separation distance ($d_v = 3.4$ Å).[9] R_c decreases asymptotically with increasing number of internanotube tunneling junctions Λ (*i.e.*, Fermi- level crossing energy bands).

MWCNT systems have been shown to exhibit remarkably large Λ values ranging between 400-500, as compared to analogous metallic SWCNT systems, which exhibit a contrastingly small number of tunneling junctions (Λ = 2).[68-69] R_c is given as follows,

$$R_c = \frac{\pi\hbar}{e^2}(\tau\Lambda)^{-1}, \quad (2)$$

where e, $\hbar$, and τ are the elementary charge, reduced Planck's constant, and tunneling probability, respectively,[9] given by

$$\tau = exp\left[-\frac{\sqrt{8m_eW_f}}{\hbar}(r - D_{outer})\right], \quad (3)$$

for $D_{outer} + d_v < r \leq D_{outer} + d_{cutoff}$, where m_e, W_f, r, d_{cutoff} and D_{outer} are the electron mass, tunneling potential barrier, interaxial separation distance between 2 neighboring MWCNTs, threshold distance beyond which tunneling effects may be neglected ($d_{cutoff} \approx 2\lambda_{Fermi}$), and MWCNT outer diameter (10 nm ± 1nm), respectively.[70] Figure 7b,c show the tunneling probability for varying potential energy barrier heights W_f (1.0 eV, 2.0 eV, and 3.0 eV) as a function of interaxial separation distance r between neighboring nanotubes and R_c as a function of Λ for varying r (10.15 nm, 10.25 nm, and 10.35 nm), respectively.

A dramatized molecular schematic cartoon of the reversible electronic transition across T_c is shown in Figure 7d (top). Figure 7d additionally exhibits a schematic cartoon of a feasible adhesive thermometric device sensitized to pyrexia-temperatures, intended only to convey the simplicity in circuitry afforded by the exceptional electronic properties exhibited by F83 and modeled on the same simplified circuitry used in the proof-of-concept demonstrations of electronic switching presented in Figure 7e (ON state) and Figure 7f (OFF state). A sourcemeter outputting a constant 2.5 V bias was used in place of a button battery with a green LED (Forward Current:

25 mA, Forward Voltage: 2.1 V) and a separate data acquisition system (Keithley 2700) wired in circuit with an RTD to measure the real-time temperature of F83 shown by the front-panel illuminated displays (Figure 7e,f) - the corresponding proof-of-concept video is provided as a supplementary media file (Video S1). The circuit diagram corresponding to Figure 7e,f is presented in Figure 7g. It is worth noting that the illumination cut-off temperature for the LED in Figure 7e,f can be further tuned by selecting an LED with specifications conforming to device requirements. More sophisticated alternative LED circuits modeled on p-type bipolar junction transistor and junction-gate field effect transistor designs using F83 as a thermometric switching component (R1) and their simulations are presented in the *Supporting Information* (Figures S20, S21, Supporting Information).

CONCLUSIONS

In MWCNT-based DCPN systems, interfacial thermal conductance between nanotube and host polymer matrix is governed by inter-phonon interactions/coupling within the nanotube and across the nanotube/host-polymer interface/interphase. Thermal conductivity of the bulk composite system is thus a corollarial manifestation of interfacial thermal energy transfer. The authors report on an alternative route towards enhancing the thermoresponsivity, electronic properties, and repeatability/reversibility in electronic phenomena of MWCNT-based DCPN systems by improving the interfacial thermal conductivity across this interfacial region through tailored covalent bridging to facilitate increased/extended phonon coupling between MWCNTs and grafted polymeric moieties through higher-frequency non-propagating vibrational modes.

In this work, PODA-*g*-MWCNTs synthesized *via* free-radical initiated RAFT polymerization of ODA onto and between the exohedral surfaces of thioester-/dithioester-

functionalized MWCNTs are reported on, where the thioester and dithioester groups function here as short-chain covalent linkers. Assembled 2.57 wt.% PODA-*g*-MWCNT samples (F83) exhibit remarkably large, repeatable, near pyrexia-sensitized positive Π values of 7,496.53 % K^{-1} ± 3,950.58 % K^{-1} at 315.1 K and low recoverable near room temperature resistance values of 246.17 Ω ± 12.19 Ω at 298.2 K. Thermal cycling between 40 consecutive ON (244.34 Ω ± 2.37 Ω)/OFF (10,043.52 Ω ± 222.40 Ω) states demonstrates exceptional repeatability/reversibility. This is effectuated by exploiting subtle form-stable, phononically-augmented 2^{nd}-order glass transition ranges, where reversible large-scale coordinated structural reorganization of extended acrylate polymer backbones transiently disrupts tunneling-assisted direct-charge transfer. An expected dependency on heating rate was observed in R(T) curves of F83 as glass transitions are kinetic processes known to depend on heating/cooling rates.

In comparison to other T-MWCNT concentrations explored in this work, F83 seemingly exhibits the optimal ratio of concentration of RAFT chain transfer agent to monomeric precursor and free-radical initiator. The results and insights from this work can be extrapolated to other nanocarbon-based DCPN systems as a facile means towards improving the thermoresponsivity, repeatability, and reversibility of desired electronic/thermal phenomena, with particular emphasis on systems sensitized to near-pyrexic and near-human body temperatures. Tunability of sensitized temperatures could potentially be attained by selecting an alkyl acrylate or other living radical polymerizable monomer with a desirable glass transition temperature. Such nanomaterials are promising candidates for human body temperature sensitized wearable thermometric sensors and other temperature sensing applications that require large electronic responses near sensing temperatures.

EXPERIMENTAL

Materials. MWCNTs (≥98% carbon basis) 6 – 8 walls thick with outer diameters of 10 nm ± 1 nm, inner diameters of 4.5 nm ± 0.5 nm, lengths (along the nanotube axis) of 3- 6 μm, and aspect ratios between 350-500 were sourced from Sigma Aldrich (synthesized by SouthWest NanoTechnologies, Inc. via catalytic chemical vapor deposition). Phosphorous pentasulfide (P_4S_{10}) (99%), octadecyl acrylate (ODA) (97%), n-hexane, and 2, 2' – azobis(2-methylpropionitrile) (AIBN) (98%) were sourced from Sigma Aldrich. Methyl alcohol (MeOH) (>98%) and methylbenzene (ACS) were obtained from Pharmco Aaper and Macron Fine Chemicals, respectively.

Synthesis of Thioester-/Dithioester-Functionalized MWCNTs. 300 mL of methylbenzene was added to 10.1 g of pristine MWCNTs (P-MWCNTs) in a 1000-mL round-bottomed flask. The resulting mixture was vigorously stirred at room temperature for 5 min followed by brief sonication at 35 kHz for 5 min. The mixture was left to stir in an Si-oil bath maintained at 323 K. Separately, 464 mg of P_4S_{10} was added to a 125-mL Erlenmeyer flask along with 150 mL of methylbenzene. The mixture was sonicated at 35 kHz for 20 min followed by heated stirring at 323 K for an additional 20 min. The P_4S_{10} mixture was slowly added to the MWCNT/methylbenzene mixture while stirring and subsequently refluxed at 388 K for 50 h. ~200mL of MeOH was slowly added to the resulting mixture under stirring to gradually reduce the temperature over ~15 min. The mixture was subsequently repeatedly washed with MeOH to dilute residual methylbenzene and centrifuged at 10,000 rpm in MeOH for 30 min three times - where the supernatant was decanted and fresh MeOH was added with each iteration. Each time fresh MeOH was added, the resulting mixture was manually churned using a glass stir rod to re-disperse the MWCNTs in solution before centrifuging. The resulting thioester-/dithioester- functionalized MWCNTs were then dried under partial vacuum at 373 K for 3 h followed by an additional 12 h at 373 K in a ventilated forced-draft oven.

Synthesis of PODA-*grafted*-MWCNTs via RAFT Polymerization. Oligomeric ODA, thioester-/dithioester-functionalized MWCNTs (T-MWCNTs), and free-radical initiator AIBN combined at different

molar ratios (Table S1, Supporting Information) were added to a 100-mL round- bottomed flask. For each set of molar ratios, 30 mL of methylbenzene was added to a separate 100-mL round-bottomed flask, septa sealed, evacuated, and degassed with dry nitrogen (N_2) for 20 min to remove any solvated gasses detrimental to the free-radical initiated living polymerization process. The 30 mL of degassed methylbenzene was transferred via canula to the dry reagents (ODA, t-MWCNTs, and AIBN) under a blanket of N_2. The mixture was refluxed at 388 K for 24 h while stirring. The resulting mixture was precipitated dropwise into MeOH at room temperature and dried under partial vacuum until a solid, uniform greyish black solid product was obtained.

Raman, FTIR, X-Ray Photoelectron, UV-Vis-NIR, and IR Spectroscopy. Raman spectra of P-MWCNTs and T-MWCNTs were obtained using a micro-Raman system with a continuous wave laser operating at an excitation wavelength of 532 nm, a x40 objective lens, and a HORIBA iHR320 spectrometer equipped with a Synapse CCD. Samples were drop cast in EtOH onto Si wafers. Fourier transform-infrared (FTIR) spectra were obtained using a Bruker Optics ALPHA-FTIR spectrophotometer in attenuated total reflection (ATR) mode outfitted with a ZnSe internal reflection element at 128 scans to average and a resolution of 2 cm^{-1}. X-ray photoelectron spectra were obtained using a Physical Electronics Model 5700 ESCA spectrometer operated at 350 W using monochromatic Al-Kα x-rays. UV-Vis-NIR spectra were obtained using an Ocean Optics HR 2000 photo-spectrometer with a deuterium/halogen light source (Ocean Optics DH-2000) in quartz cuvettes. Direct IR absorbance spectra were obtained using a nanoIR2™ system (Anasys Instruments Corp.) equipped with an optical parametric oscillating (OPO) laser as an IR source.

Field-Emission Scanning Electron, Atomic Force, and Scanning Thermal Microscopy. Scanning electron micrographs were obtained using a Carl Zeiss LEO 1525 field-emission scanning electron microscope outfitted with a GEMINI field-emission column. Micrographs were obtained at accelerating potentials ranging between 2-15 kV and comparatively short working distances. Atomic force microscopy (AFM) and scanning thermal microscopy (SThM) micrographs were obtained using a nanoIR2™ AFM-IR system (Anasys Instruments Corp.) outfitted with an AFM- based Thermalever™ probe with a tip radius of

<30 nm, a tip height of 10 μm, and a cantilever length of 150 μm in a Wheatstone bridge configuration using an OPO laser as a mid-IR source.

Field-Emission Transmission Electron Microscopy. Samples for transmission electron microscopy (TEM) characterization were prepared by dispersing F83 in n-hexane at a concentration of 0.1 % (wt./v.) and bath sonicating at 35 kHz for 2 min prior to dropping directly onto a holey-C-coated Cu-grid (200 mesh, Ted Pella) atop medium-flow filter paper and air-dried at STP for 30 min prior to loading into the TEM sample chamber and pumping down. Samples were characterized using a JEOL JEM-2010-F field-emission transmission-electron microscope operating at an accelerating voltage of 200 keV.

Thermogravimetric and Differential Calorimetric Analysis. Simultaneous thermogravimetric and differential calorimetric analyses were conducted on powdered samples using a TA Instruments SDT Q600. The sensitivity of the instrument (differential thermal analyzer) is 0.001 °C. Linear ramping cycles from 300 – 1270 K at a heating rate of 10 °C/min under Ar at a flow rate of 50 mg/mL were conducted and measured in alumina pans. ΔH values were calculated by numerically integrating DSC curves across phase transitions for standardized baseline ranges.

***I-V* Characterization.** A manual probe station (JR-2727) comprised of two KRN-09S probe positioners (J Micro Technologies) fitted with PtIr needle-tip electrodes were used for two-probe temperature- dependent *I-V* characterization. A stable heat source constructed from a hotplate (Corning PD-400D) outfitted with a symmetrical rectangular cuboid steel plate 13 mm in thickness in direct thermal contact with the hotplate to regulate and homogenize heat flow and distribution across measuring areas. PODA-*g*-MWCNT samples were drop cast between pairs of thin-film Au electrodes thermally evaporated onto glass substrates under high-vacuum with interelectrode gaps of ~200 μm. Profilometry techniques to characterize the dimensionality of the electrodes were not requisite as the conductivities of synthesized materials are not reported on in this work. A Keithley 2400 SourceMeter was used to drive linear DC voltage sweeps from 1 – 2 V at a step potential of 0.04 V and record responsive temperature-dependent current-resistance values across linear heating and exponential cooling cycles, with the real-time

temperature of the sample being concomitantly measured and recorded using a Pt-RTD sensor (PT100, Omega Engineering, Uncertainty: ±0.12% @ 273 K) in circuit with a Keithley 2700 Data Acquisition Unit.

ASSOCIATED CONTENT

Supporting Information

The Supporting Information is available free of charge on the ACS Publications website at DOI:

Syntheses schemes for PODA-*g*-MWCNTs; experimental RTD positioning, heating rate calibration, and sources of background error; temperature-dependent *I-V* characterization and Π of F83, F8C, F86, and F87; TGA of F80, F83, and F86; theoretical device circuit diagrams and simulations; temperature-dependent dimensional swelling characteristics of F83; AFM-IR analysis of F83, Raman spectra of pristine, oxidized, and thiolated MWCNTs; Raman, IR-absorbance, and XPS spectra of F80, F83, and F86 (PDF)

Video S1: Electronic switching in LED circuit (MP4)

AUTHOR INFORMATION

Corresponding Author

*E-Mail (A. J. Wang): awang8@uh.edu

ORCID

Alexander J. Wang: 0000-0002-4991-0692

Surendra Maharjan: 0000-0003-0117-3344

Kang-Shyang Liao: 0000-0001-9617-4977

Brian P. McElhenny: 0000-0001-5403-8723

Zhuan Zhu: 0000-0003-4377-9053

Shuo Chen: 0000-0002-7145-1269

Andrew R. Barron: 0000-0002-2018-8288

Oomman K. Varghese: 0000-0003-2386-0153

Jiming Bao: 0000-0002-6819-0117

Notes

The authors declare no competing financial interest.

ACKNOWLEDGMENT

Dr. Andrew R. Barron acknowledges support from The Robert A. Welch Foundation (C-0002). Dr. Jiming Bao acknowledges support from The Robert A. Welch Foundation (E-1728). Dr. Shuo Chen acknowledges support from the State of Texas through the Texas Center for Superconductivity at the University of Houston.

REFERENCES

(1) Curran, S. A.; Ajayan, P. M.; Blau, W. J.; Carroll, D. L.; Coleman, J. N.; Dalton, A. B.; Davey, A. P.; Drury, A.; McCarthy, B.; Maier, S.; Strevens, A. A Composite from Poly(m-phenylenevinylene-co-2,5-dioctoxy-p-phenylenevinylene) and Carbon Nanotubes: A Novel Material for Molecular Optoelectronics. *Advanced Materials* **1998,** *10* (14), 1091-1093.

(2) Ajayan, P. M.; Stephan, O.; Colliex, C.; Trauth, D. Aligned Carbon Nanotube Arrays Formed by Cutting a Polymer Resin-Nanotube Composite. *Science* **1994,** *265* (5176), 1212-1214.

(3) Fadel, T. R.; Sharp, F. A.; Vudattu, N.; Ragheb, R.; Garyu, J.; Kim, D.; Hong, E.; Li, N.; Haller, G. L.; Pfefferle, L. D.; Justesen, S.; Herold, K. C.; Fahmy, T. M. A carbon nanotube–polymer composite for T-cell therapy. *Nature Nanotechnology* **2014,** *9*, 639.

(4) Torrisi, F.; Coleman, J. N. Electrifying inks with 2D materials. *Nature Nanotechnology* **2014,** *9*, 738.

(5) Sekitani, T.; Nakajima, H.; Maeda, H.; Fukushima, T.; Aida, T.; Hata, K.; Someya, T. Stretchable active-matrix organic light-emitting diode display using printable elastic conductors. *Nature Materials* **2009,** *8*, 494.
(6) Yamada, T.; Hayamizu, Y.; Yamamoto, Y.; Yomogida, Y.; Izadi-Najafabadi, A.; Futaba, D. N.; Hata, K. A stretchable carbon nanotube strain sensor for human-motion detection. *Nature Nanotechnology* **2011,** *6*, 296.
(7) Maharjan, S.; Liao, K.-S.; Wang, A. J.; Zhu, Z.; Alam, K.; McElhenny, B. P.; Bao, J.; Curran, S. A. Functionalized few-layered graphene oxide embedded in an organosiloxane matrix for applications in optical limiting. *Chemical Physics Letters* **2019,** *714*, 149-155.
(8) Liao, K.-S.; Wan, A.; Batteas, J. D.; Bergbreiter, D. E. Superhydrophobic Surfaces Formed Using Layer-by-Layer Self-Assembly with Aminated Multiwall Carbon Nanotubes. *Langmuir* **2008,** *24* (8), 4245-4253.
(9) Wang, A. J.; Liao, K.-S.; Maharjan, S.; Zhu, Z.; McElhenny, B.; Bao, J.; Curran, S. A. Percolating conductive networks in multiwall carbon nanotube-filled polymeric nanocomposites: towards scalable high-conductivity applications of disordered systems. *Nanoscale* **2019,** *11* (17), 8565-8578.
(10) Curran, S. A.; Talla, J.; Dias, S.; Donghui, Z.; Carroll, D.; Birx, D. Electrical transport measurements of highly conductive carbon nanotube/poly(bisphenol A carbonate) composite.(Technical report). *Journal of Applied Physics* **2009,** *105* (7), 073711-1-073711-5.
(11) Kinloch, I. A.; Suhr, J.; Lou, J.; Young, R. J.; Ajayan, P. M. Composites with carbon nanotubes and graphene: An outlook. *Science* **2018,** *362* (6414), 547.
(12) Yang, H.; Qi, D.; Liu, Z.; Chandran, B. K.; Wang, T.; Yu, J.; Chen, X. Soft Thermal Sensor with Mechanical Adaptability. *Advanced Materials* **2016,** *28* (41), 9175-9181.
(13) Chen, Z.; Hsu, P.-C.; Lopez, J.; Li, Y.; To, J. W. F.; Liu, N.; Wang, C.; Andrews, Sean C.; Liu, J.; Cui, Y.; Bao, Z. Fast and reversible thermoresponsive polymer switching materials for safer batteries. *Nature Energy* **2016,** *1*, 15009.
(14) Yang, H.; Leow, W. R.; Chen, X. Thermal-Responsive Polymers for Enhancing Safety of Electrochemical Storage Devices. *Advanced Materials* **2018,** *30* (13), 1704347.
(15) Wang, C.; Wang, C.; Huang, Z.; Xu, S. Materials and Structures toward Soft Electronics. *Advanced Materials* **2018,** *30* (50), 1801368.
(16) Zhang, X.; Bellan, L. M. Composites Formed from Thermoresponsive Polymers and Conductive Nanowires for Transient Electronic Systems. *ACS Applied Materials & Interfaces* **2017,** *9* (26), 21991-21997.
(17) Yokota, T.; Inoue, Y.; Terakawa, Y.; Reeder, J.; Kaltenbrunner, M.; Ware, T.; Yang, K.; Mabuchi, K.; Murakawa, T.; Sekino, M.; Voit, W.; Sekitani, T.; Someya, T. Ultraflexible, large-area, physiological temperature sensors for multipoint measurements. *Proceedings of the National Academy of Sciences* **2015,** *112* (47), 14533.
(18) Fernandes, G. E.; Kim, J. H.; Sood, A. K.; Xu, J. Giant Temperature Coefficient of Resistance in Carbon Nanotube/Phase-Change Polymer Nanocomposites. *Advanced Functional Materials* **2013,** *23* (37), 4678-4683.
(19) Wang, Y.; Mi, H.; Zheng, Q.; Ma, Z.; Gong, S. Graphene/Phase Change Material Nanocomposites: Light-Driven, Reversible Electrical Resistivity Regulation via Form-Stable Phase Transitions. *ACS Applied Materials & Interfaces* **2015,** *7* (4), 2641-2647.
(20) Kholmanov, I.; Kim, J.; Ou, E.; Ruoff, R. S.; Shi, L. Continuous Carbon Nanotube–Ultrathin Graphite Hybrid Foams for Increased Thermal Conductivity and Suppressed Subcooling in Composite Phase Change Materials. *ACS Nano* **2015,** *9* (12), 11699-11707.

(21) Zheng, R.; Gao, J.; Wang, J.; Chen, G. Reversible temperature regulation of electrical and thermal conductivity using liquid–solid phase transitions. *Nature Communications* **2011,** *2*, 289.
(22) Sun, P. C.; Wu, Y. L.; Gao, J. W.; Cheng, G. A.; Chen, G.; Zheng, R. T. Room Temperature Electrical and Thermal Switching CNT/Hexadecane Composites. *Advanced Materials* **2013,** *25* (35), 4938-4943.
(23) Jeon, J.; Lee, H.-B.-R.; Bao, Z. Flexible Wireless Temperature Sensors Based on Ni Microparticle-Filled Binary Polymer Composites. *Advanced Materials* **2013,** *25* (6), 850-855.
(24) Cui, X.; Chen, J.; Zhu, Y.; Jiang, W. Lightweight and conductive carbon black/chlorinated poly(propylene carbonate) foams with a remarkable negative temperature coefficient effect of resistance for temperature sensor applications. *Journal of Materials Chemistry. C* **2018,** *6* (35), 9354-9362.
(25) Lee, S.-E.; Moon, K.-S.; Sohn, Y. Temperature dependence of contact resistance at metal/MWNT interface. *Applied Physics Letters* **2016,** *109* (2), 021605.
(26) Yan, C.; Wang, J.; Lee, P. S. Stretchable Graphene Thermistor with Tunable Thermal Index. *ACS Nano* **2015,** *9* (2), 2130-2137.
(27) Hutchison, J. S.; Ward, R. E.; Lacroix, J.; Hébert, P. C.; Barnes, M. A.; Bohn, D. J.; Dirks, P. B.; Doucette, S.; Fergusson, D.; Gottesman, R.; Joffe, A. R.; Kirpalani, H. M.; Meyer, P. G.; Morris, K. P.; Moher, D.; Singh, R. N.; Skippen, P. W.; Hypothermia Pediatric Head Injury Trial, I.; the Canadian Critical Care Trials, G. Hypothermia therapy after traumatic brain injury in children. *The New England Journal of Medicine* **2008,** *358* (23), 2447-2456.
(28) Shah, N. T.; Habtegebriel, Y. A.; Bloomfield, D. A. Extreme Hyperpyrexia of Uncertain Origin. *The Journal of Emergency Medicine* **2016,** *51* (3), e33-e35.
(29) Dusen, M. S. V. Platinum-resistance thermometry at low temperatures. *Journal of the American Chemical Society* **1925,** *47* (2), 326-332.
(30) Thornton, S. T. *Modern physics for scientists and engineers*, Fourth edition. ed.; Boston, MA : Brooks Cole/Cengage Learning: 2013.
(31) Mehmood, Z.; Mansoor, M.; Haneef, I.; Ali, S. Z.; Udrea, F. Evaluation of thin film p-type single crystal silicon for use as a CMOS Resistance Temperature Detector (RTD). *Sensors and Actuators A: Physical* **2018,** *283*, 159-168.
(32) Zhang, J.; Nagao, Y.; Kuwano, S.; Ito, Y. Microstructure and Temperature Coefficient of Resistance of Platinum Films. *Japanese Journal of Applied Physics* **1997,** *36* (Part 1, No. 2), 834-839.
(33) Bakker, A. *High-accuracy CMOS smart temperature sensors*, Boston, MA : Kluwer Academic Publishers: 2000.
(34) Morris Alan, S.; Langari, R. *Temperature Measurement*, Elsevier: 2012; p 1-2.
(35) Cheng, S.; Tom, K.; Pecht, M. Failure Precursors for Polymer Resettable Fuses. *IEEE Transactions on Device and Materials Reliability* **2010,** *10* (3), 374-380.
(36) Shen, L.; Wang, F. Q.; Yang, H.; Meng, Q. R. The combined effects of carbon black and carbon fiber on the electrical properties of composites based on polyethylene or polyethylene/polypropylene blend. *Polymer Testing* **2011,** *30* (4), 442-448.
(37) Curran, S.; Liao, K.-S.; Wang, A., Graft polymerization initiated on graphitic nanomaterials and their nanocomposite formation. US Patent 9,688,538 B2.
(38) Čech, J.; Curran, S. A.; Zhang, D.; Dewald, J. L.; Avadhanula, A.; Kandadai, M.; Roth, S. Functionalization of multi-walled carbon nanotubes: Direct proof of sidewall thiolation. *Physica Status Solidi (b)* **2006,** *243* (13), 3221-3225.

(39) Cowie, J. M. G.; Arrighi, V. *Polymers: chemistry and physics of modern materials*, CRC press: 2007.
(40) Sudalai, A.; Kanagasabapathy, S.; Benicewicz, B. C. Phosphorus pentasulfide: A mild and versatile catalyst/reagent for the preparation of dithiocarboxylic esters. *Organic Letters* **2000,** *2* (20), 3213-3216.
(41) Ozturk, T.; Ertas, E.; Mert, O. A Berzelius Reagent, Phosphorus Decasulfide (P4S10), in Organic Syntheses. *Chemical Reviews* **2010,** *110* (6), 3419-3478.
(42) Curran, S. A.; Cech, J.; Zhang, D.; Dewald, J. L.; Avadhanula, A.; Kandadai, M.; Roth, S. Thiolation of carbon nanotubes and sidewall functionalization. *Journal of Materials Research* **2006,** *21* (4), 1012-1018.
(43) Gautam, K. S.; Dhinojwala, A. Melting at Alkyl Side Chain Comb Polymer Interfaces. *Physical Review Letters* **2002,** *88* (14), 145501.
(44) Qin, S.; Matyjaszewski, K.; Xu, H.; Sheiko, S. S. Synthesis and Visualization of Densely Grafted Molecular Brushes with Crystallizable Poly(octadecyl methacrylate) Block Segments. *Macromolecules* **2003,** *36* (3), 605-612.
(45) Scott, T. H.; David, G. C.; Sergei, S.; Liping, X.; Rahmi, O.; Paul, B.; Monica, U.; Michael, S. S.; Giles, S.; Moonsub, S.; Pawel, K. Interfacial heat flow in carbon nanotube suspensions. *Nature Materials* **2003,** *2* (11), 731.
(46) Yang, J.; Yang, Y.; Waltermire, S. W.; Gutu, T.; Zinn, A. A.; Xu, T. T.; Chen, Y.; Li, D. Measurement of the Intrinsic Thermal Conductivity of a Multiwalled Carbon Nanotube and Its Contact Thermal Resistance with the Substrate. *Small* **2011,** *7* (16), 2334-2340.
(47) Williams; Maris. Numerical study of phonon localization in disordered systems. *Physical Review. B, Condensed matter* **1985,** *31* (7), 4508-4515.
(48) Ding, H.; Wei, J.-S.; Xiong, H.-M. Nitrogen and sulfur co-doped carbon dots with strong blue luminescence. *Nanoscale* **2014,** *6* (22), 13817-13823.
(49) Wang, X.; Zhang, Z.; Yan, X.; Qu, Y.; Lai, Y.; Li, J. Interface polymerization synthesis of conductive polymer/graphite oxide@sulfur composites for high-rate lithium-sulfur batteries. *Electrochimica Acta* **2015,** *155*, 54-60.
(50) Wiles, D. M.; Gingras, B. A.; Suprunchuk, T. The C=S stretching vibration in the infrared spectra of some thiosemicarbazones. *Canadian Journal of Chemistry* **1967,** *45* (5), 469-473.
(51) Kim, G.-H.; Lee, D.; Shanker, A.; Shao, L.; Kwon, M. S.; Gidley, D.; Kim, J.; Pipe, K. P. High thermal conductivity in amorphous polymer blends by engineered interchain interactions. *Nature Materials* **2015,** *14* (3), 295-300.
(52) Peter, J. O. b.; Sergei, S.; Jianxiun, L.; Philippe, K. C.; Danielle, L.; Mutin, P. H.; Masashi, Y.; Pawel, K.; Ganpati, R. Bonding-induced thermal conductance enhancement at inorganic heterointerfaces using nanomolecular monolayers. *Nature Materials* **2012,** *12* (2), 118.
(53) Oçafrain, M.; Tran, T. K.; Blanchard, P.; Lenfant, S.; Godey, S.; Vuillaume, D.; Roncali, J. Electropolymerized Self-Assembled Monolayers of a 3,4-Ethylenedioxythiophene-Thiophene Hybrid System. *Advanced Functional Materials* **2008,** *18* (15), 2163-2171.
(54) Sodhi, R. N. S.; Cavell, R. G. KLL auger and core level (1s and 2p) photoelectron shifts in a series of gaseous sulfur compounds. *Journal of Electron Spectroscopy and Related Phenomena* **1986,** *41* (1), 1-24.
(55) Song, J.-G.; Ryu, G. H.; Lee, S. J.; Sim, S.; Lee, C. W.; Choi, T.; Jung, H.; Kim, Y.; Lee, Z.; Myoung, J.-M.; Dussarrat, C.; Lansalot-Matras, C.; Park, J.; Choi, H.; Kim, H. Controllable synthesis of molybdenum tungsten disulfide alloy for vertically composition-controlled multilayer. *Nature Communications* **2015,** *6*, 7817.

(56) Park, H.; Lee, S. H.; Kim, F. S.; Choi, H. H.; Cheong, I. W.; Kim, J. H. Enhanced thermoelectric properties of PEDOT:PSS nanofilms by a chemical dedoping process. *Journal of Materials Chemistry A* **2014,** *2* (18), 6532-6539.
(57) Ozaki, Y.; Storer, A. C.; Carey, P. R. The Raman and resonance Raman spectra of some substituted dialkyl dithioesters and their rotational isomers. *Canadian Journal of Chemistry* **1982,** *60* (2), 190-198.
(58) Rong, W.; Fan, Z.; Yu, Y.; Bu, H.; Wang, M. Influence of entanglements on glass transition of atactic polystyrene. *Journal of Polymer Science Part B: Polymer Physics* **2005,** *43* (16), 2243-2251.
(59) Jombert, A. S.; Coleman, K. S.; Wood, D.; Petty, M. C.; Zeze, D. A. Poole–Frenkel conduction in single wall carbon nanotube composite films built up by electrostatic layer-by-layer deposition. *Journal of Applied Physics* **2008,** *104* (9), 094503.
(60) Joung, D.; Chunder, A.; Zhai, L.; Khondaker, S. I. Space charge limited conduction with exponential trap distribution in reduced graphene oxide sheets. *Applied Physics Letters* **2010,** *97* (9), 093105.
(61) Sibatov, R.; Shulezhko, V.; Svetukhin, V. Fractional Derivative Phenomenology of Percolative Phonon-Assisted Hopping in Two-Dimensional Disordered Systems. *Entropy* **2017,** *19* (9), 463.
(62) Sarker, B. K.; Khondaker, S. I. Thermionic Emission and Tunneling at Carbon Nanotube–Organic Semiconductor Interface. *ACS Nano* **2012,** *6* (6), 4993-4999.
(63) Keys, A. S.; Garrahan, J. P.; Chandler, D. Calorimetric glass transition explained by hierarchical dynamic facilitation. *Proceedings of the National Academy of Sciences* **2013,** *110* (12), 4482.
(64) Moynihan, C. T.; Easteal, A. J.; Wilder, J.; Tucker, J. Dependence of the glass transition temperature on heating and cooling rate. *The Journal of Physical Chemistry* **1974,** *78* (26), 2673-2677.
(65) Gibbs, J. H.; Dimarzio, E. A. Nature of the Glass Transition and the Glassy State. *The Journal of Chemical Physics* **1958,** *28* (3), 373-383.
(66) Jackle, J. Models of the glass transition. *Reports on Progress in Physics* **1986,** *49* (2), 171-231.
(67) Turnbull, D.; Cohen, M. H. Free-Volume Model of the Amorphous Phase: Glass Transition. *The Journal of Chemical Physics* **1961,** *34* (1), 120-125.
(68) Li, H. J.; Lu, W. G.; Li, J. J.; Bai, X. D.; Gu, C. Z. Multichannel ballistic transport in multiwall carbon nanotubes. *Physical Review Letters* **2005,** *95* (8), 086601.
(69) Gong, S.; Zhu, Z. H.; Haddad, E. I. Modeling electrical conductivity of nanocomposites by considering carbon nanotube deformation at nanotube junctions. *Journal of Applied Physics* **2013,** *114* (7), 074303.
(70) Bao, W. S.; Meguid, S. A.; Zhu, Z. H.; Weng, G. J. Tunneling resistance and its effect on the electrical conductivity of carbon nanotube nanocomposites. *Journal of Applied Physics* **2012,** *111* (9), 093726.

SYNOPSIS

Optimizing thermal conductance across the nanocarbon-filler/host-polymer matrix interface in polymer nanocomposites is critical towards realizing thermoresponsive, repeatable, and reversible electronic switching phenomena in such disordered systems. In this work, near hyperpyrexia-sensitized thermometric nanocomposites of poly(octadecyl acrylate)-*grafted*-multiwall carbon nanotubes (PODA-*g*-MWCNTs) are reported on. Synthesized PODA-*g*-MWCNTs exhibit exceptionally large, repeatable, and reversible electronic switching properties across form-stable glass transition ranges near hyperpyrexic temperatures facilitated through covalent tailoring of the MWCNT/PODA interface/interphase and are promising candidates for wearable human body thermometric sensors/switches.